NANO LETTERS

pubs.acs.org/NanoLett

Letter

Direct Hydrogen Production Promoted by Laser-Induced Water Plasma

Qunfang Gu,[#] Yimin Zhang,[#] Daqiang Chen, Luhao Zhang, Jiyu Xu,* Cui Zhang,* Sheng Meng,* and Enge Wang*

Cite This: *Nano Lett.* 2024, 24, 12799−12805

Read Online

ACCESS | Metrics & More | Article Recommendations | Supporting Information

ABSTRACT: Hydrogen, as a clean energy carrier, plays an important role in addressing the current energy and environmental crisis. However, conventional hydrogen production technologies require extreme reaction conditions, such as high temperature, high pressure, and catalysts. Herein, we study the microscopic mechanism of laser-induced water plasma and subsequent H_2 production with real-time time-dependent density functional theory simulations and *ab initio* molecular dynamics simulations. The results demonstrate that intense laser excites liquid water to generate nonequilibrium plasma in a warm-dense state, which constitutes a superior reaction environment. Subsequent annealing leads to the recombination of energetic reactive particles to generate H_2, O_2, and H_2O_2 molecules. Annealing rate and laser wavelength are shown to modulate the product ratio, and the energy conversion efficiency can reach ∼9.2% with an annealing rate of 1.0 K/fs. This work reveals the nonequilibrium atomistic mechanisms of hydrogen production from laser-induced water plasma and shows far-reaching implications for the design of optically controllable hydrogen technology.

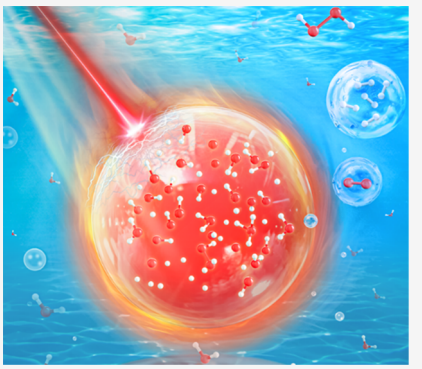

KEYWORDS: *laser-induced water plasma, hydrogen production, nonadiabatic molecular dynamics, ultrafast annealing*

Given the current challenges of global climate change and diminishing fossil fuel reserves, there is an urgent need for the development of sustainable and environmentally friendly energy sources. Hydrogen, owing to its ability to supply energy without emitting greenhouse gases, is considered to play a vital role for a greener and more sustainable future.[1−3] In recent years, hydrogen production based on water splitting has been widely investigated. However, conventional methods such as water electrolysis,[4] thermochemical water decomposition,[5,6] and photocatalytic water splitting,[7−9] suffer from extreme reaction conditions of high temperature and high pressure, or require specific catalytic environments and noble metal catalysts. This leads to realistic issues of high costs, environmental pollution, and low conversion efficiencies. Therefore, it is necessary to design novel strategies for green and efficient hydrogen gas prodcution.[10]

It was found that the intense laser pulses can violently excite liquid water[11,12] and lead to ultrafast plasma generation in liquid water.[13] The generation of water plasma is highly beneficial for laser-based catalysis, synthesis, and manufacture in heterogeneous systems. On the other hand, the water plasma also constitutes a highly active environment for hydrogen production in pure water. For example, Chin and Lagacé[14] investigated the formation of H_2 from water splitting by the intense femtosecond pulses and detected the ultimate products of H_2, O_2, and H_2O_2 with no specific stoichiometry. Then, Maatz et al.[15] demonstrated the production of H_2 and O_2 with a ratio of 2:1 from laser-irradiated aqueous systems. Under appropriate irradiation conditions, Pawlak et al.[16] achieved the selective production of H_2 and H_2O_2 (without O_2) from liquid water. Despite these experimental observations, the microscopic mechanisms of water plasma generation, e.g., active species, charge transfers, and reaction pathways, are still illusive due to the complex interactions and ultrafast timescales. A comprehensive study of photoinduced ultrafast nonequilibrium dynamics, including plasma generation and ultrafast annealing, is highly desired for understanding and modulating photoinduced gas production.

Here, we investigate the microscopic mechanism of laser-induced H_2 production from nonequilibrium water plasma with the real-time time-dependent density functional theory (rt-TDDFT)[17,18] simulations and *ab initio* molecular dynamics (AIMD) simulations. We find that the laser-induced hydrogen production from water plasma can be divided into the steps of violent water dissociation and subsequent hydrogen recombination processes, as shown in Figure 1. The intense laser irradiation triggers the photoionization of a large portion of

Received: June 25, 2024
Revised: September 25, 2024
Accepted: September 30, 2024
Published: October 3, 2024

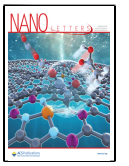

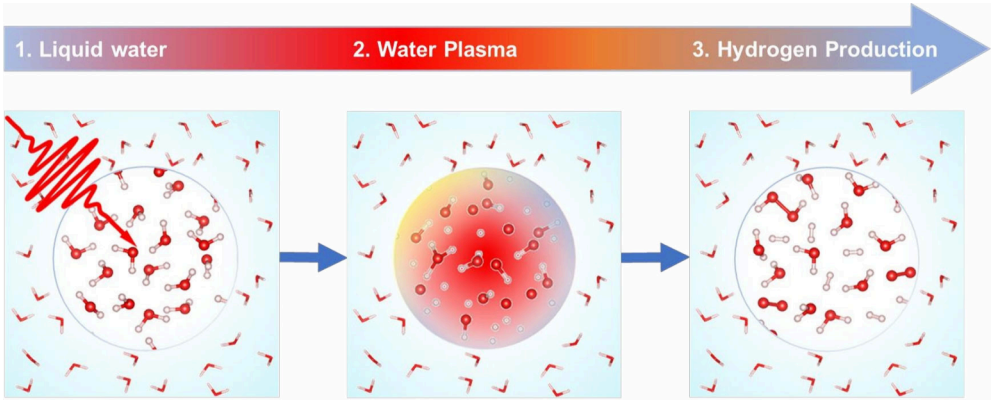

Figure 1. Schematic of laser-induced plasma in liquid water to produce hydrogen molecules. The initial liquid water is excited by the laser pulses and violently decomposes into various energetic chemical groups, forming water plasma at the femtosecond timescale. Then the ultrafast annealing process promotes the retention of desired products (H_2, O_2, and H_2O_2) at a picosecond timescale, and an absorbed photon-to-chemical energy conversion efficiency of up to 9.2% is achieved.

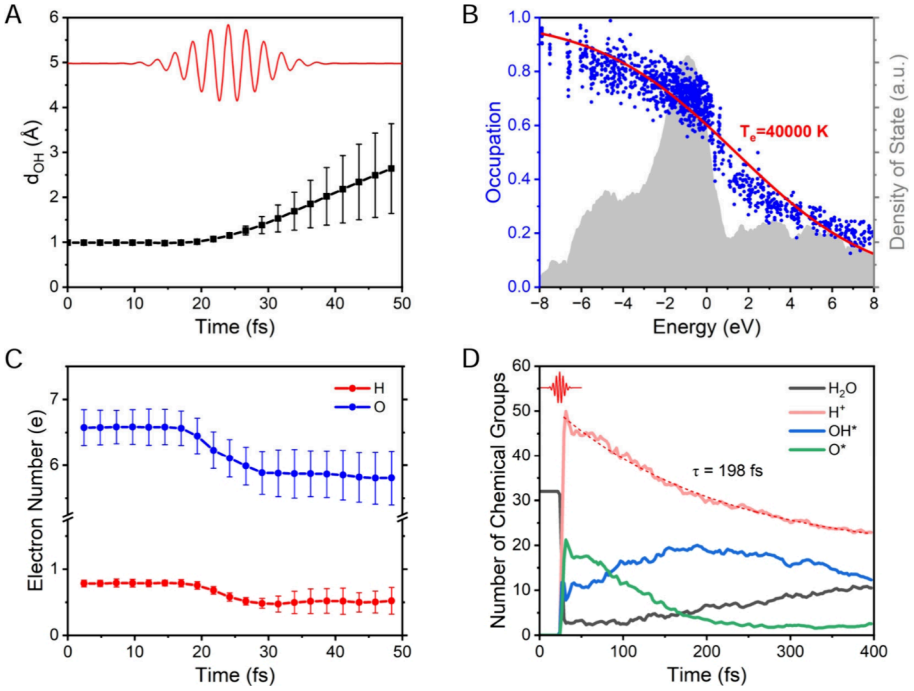

Figure 2. Rt-TDDFT simulations of water plasma generation and ultrafast relaxations at a femtosecond timescale. (A) Temporal evolutions of averaged O−H distances of initial water molecules. The electric field of the laser pulses is also shown. (B) The electronic occupation and instantaneous electronic density of states at t = 50 fs, which is averaged with 8 independent trajectories. (C) The electrons on hydrogen and oxygen nuclei during the first 50 fs of rt-TDDFT simulations. (D) Temporal evolution of active particles during photoexcitation with λ = 800 nm and E_0 = 2.4 V/Å.

water molecules and gives rise to ultrafast formation of water plasma comprising various energetic chemical groups at the femtosecond timescale. The plasma state provides an active environment for the subsequent generation of H_2, O_2, and H_2O_2 molecules via the recombination of respective radicals within several picoseconds. The wavelength of the laser pulses plays a crucial role in the excitation of water molecules and directly affects the generation efficiency of water plasma. The ultrafast annealing inhibits the reactions of energetic chemical groups recombining back into water molecules and promotes the yield of useful products. A high absorbed photon-to-chemical energy conversion of 9.2% is obtained with an annealing rate of 1.0 K/fs. Our results provide a realistic method for H_2 generation from laser-induced water plasma without any catalyst and reveal the underlying microscopic dynamic mechanism, which is of great significance to realize efficient hydrogen production by femtosecond laser pulses.

The laser-induced water plasma generation spans several characteristic timescales[19] and includes several elemental processes, e.g., photoexcitation, water dissociation, heating, and cooling. Here, we adopt the combined simulation strategies to study the generation and subsequent annealing of laser-induced water plasma from femtosecond to picosecond timescales. The nonadiabatic rt-TDDFT simulation is employed to simulate the photoexcited water plasma generation at a femtosecond timescale, and the finite-temperature (T_i)-based AIMD[20] annealing simulations are used to simulate the subsequent cooling processes at a

https://doi.org/10.1021/acs.nanolett.4c02996
Nano Lett. 2024, 24, 12799−12805

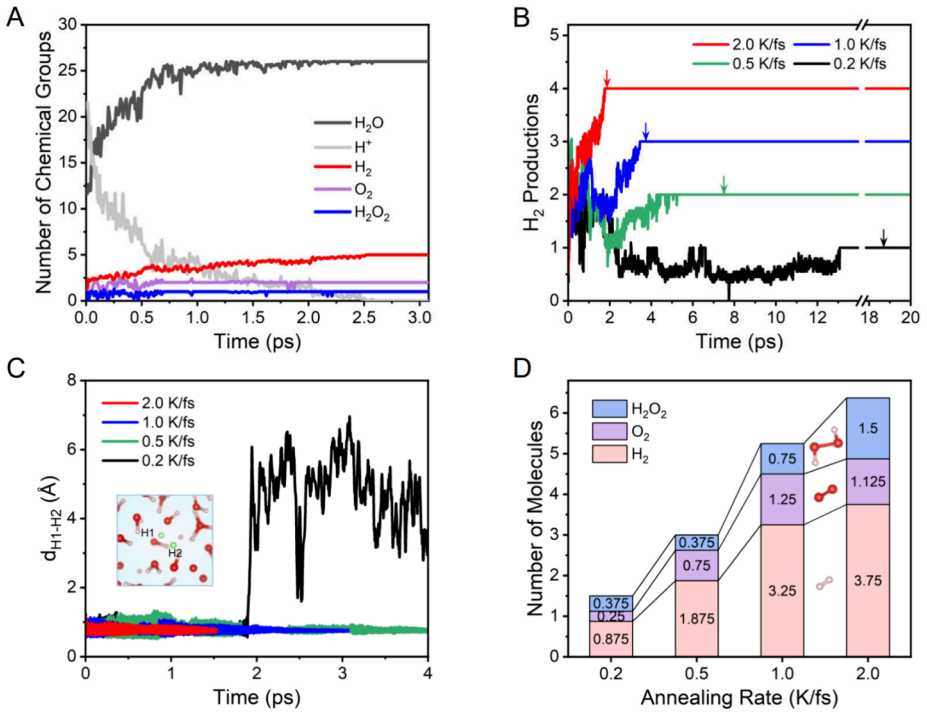

Figure 3. Annealing simulations and molecule formations during cooling processes. (A) Temporal evolutions of the numbers of various components with an annealing rate of 1.0 K/fs (traj1 in Table S1). The final configuration of the rt-TDDFT simulations was chosen as the initial state for the annealing simulation. (B) Temporal evolutions of H_2 production under different annealing rates with the same initial configuration (traj8 in Table S1). The arrows denote the end times of annealing simulations. (C) The distance between H1−H2 atoms (marked in green in the inset) is different with different annealing rates. (D) The averaged molecular productions with different annealing rates. The pink, purple, and blue regions denote H_2, O_2, and H_2O_2 molecules, respectively.

picosecond scale. In experiments, the nonequilibrium water plasma can couple with the external environments at the picosecond timescale;[19] thus, the nonequilibrium water plasma intrinsically undergoes ultrafast annealing processes to give rise to energy dissipation during picosecond-long cooling processes. What's more, additional experimental operations, e.g., passing an inert gas stream[21] or applying an electric field,[22] can further accelerate the cooling processes of water plasma.

We chose the laser pulse with a Gaussian envelope to excite liquid water in rt-TDDFT simulations in Figure 2A, and the laser wavelength is 800 nm with a maximum electric field strength of 2.4 V/Å. Similar simulation setups were used in our previous work.[13] A total of eight trajectories are simulated to give the converged evolutions following photoexcitation. Figure S1A shows the temporal evolutions of the electronic excitation of photoexcited liquid water. The valence electrons are promoted to the conduction band during the irradiation of laser pulses, and then the photoexcited electrons and holes recombine in the subsequent relaxation processes. The excited valence electrons reach ∼16% at t = 50 fs, which is large enough to trigger the ultrafast water plasma generation in liquid water,[13] and the tunneling ionization accounts for the electronic excitation processes here.[13,23,24] Figure 2B shows the instantaneous electronic occupation and the electronic density of states at t = 50 fs. One can see that the electronic occupation presents a Fermi−Dirac distribution with an electronic temperature T_e of ∼40000 K. The bandgap is closed, indicating that a metallicity occurs.

The intense electronic excitations lead to a violent response of ionic subsystems. The bonds of water molecules are greatly stretched during the laser pulses (Figure 2A), and water molecules dissociate to generate various chemical groups or particles, such as H^+, OH*, O*, H_3O^+, and HOO*. Figure 2C shows that the hydrogen nuclei lose electrons upon photoexcitation, and the number of electrons of oxygen nuclei decreases from ∼6.6 to ∼6 e, demonstrating the emergence of O* radicals. These active species can recombine to generate various transient chemical groups or molecules.

Figure 2D exhibits the numbers of various particles in rt-TDDFT simulations, and a three-stage relaxation process of energetic particles is obtained following photoexcitation. In stage I, a large number of free H^+ and O* combine to generate OH*, and the changes of these particle numbers have a ratio of 1:1:1. The number of water molecules remains unchanged. In stage II, the free H^+ combines with adjacent OH* and OH* equally. The changes in particle numbers of H^+ and O* have a ratio of 2:1. The number of OH* seems unchanged; the number of water molecules increases; and O* is almost exhausted in this stage. In stage III, H^+ ions mainly recombine with OH* to form water molecules. The depletion of free hydrogen ions shows an exponential decay with a time constant of ∼198 fs. The variations of particle numbers are consistent with those from charge analysis of oxygen and hydrogen nuclei (Figure S2). The emergence of O* and OH* radicals is consistent with experimental measurements.[14] We note that a few other particles (H_3O^+, HOO*) and transient molecules (H_2, O_2, H_2O_2) are also generated (Figure S3A), and Figure S3B shows an instantaneous structure at t = 400 fs. The main processes of H^+ recombination can be represented by the following reactions:

$$H^+ + O^* + e^- \rightarrow OH^* \quad (1)$$

https://doi.org/10.1021/acs.nanolett.4c02996
Nano Lett. 2024, 24, 12799−12805

$$H^+ + OH^* + e^- \rightarrow H_2O \quad (2)$$

After the ultrafast relaxation of highly nonequilibrium water plasma within 400 fs, the ionic subsystems are heated and reach a high ionic temperature of more than 3000 K (Figure S1B). At the same time, the electronic subsystems undergo the corresponding cooling processes due to the energy transfer to ionic subsystems (Figure S1B). The nonequilibrium electronic and ionic subsystems still have two different "effective temperatures" of $\sim 10^4$ and $\sim 10^3$ K, respectively.

The Gibbs free energy barriers of molecular dissociation reactions (as a function of temperature) can give important implications for subsequent relaxation processes.[25] As shown in Figure S4, the high temperatures stabilize the severe dissociative configurations of water plasma, and the active particles can recombine to generate various molecules with the cooling of water plasma. At the same time, the energy zero point of H_2O dissociation lies at a higher temperature than those of H_2 and H_2O_2 dissociation, which suggests that the active radicals of water plasma prefer to recombine into H_2O molecules during extremely slow cooling processes. On the other hand, the ultrafast annealing processes may enhance these secondary recombination reactions and retain the possible H_2 and H_2O_2 molecules during the ultrafast cooling processes of water plasma. Therefore, the annealing rate v_a of water plasma can be a key factor affecting the reaction pathways and the species of products. We employ the T_i-based AIMD simulations to simulate the long-time cooling processes of water plasma at the picosecond timescales. The final configurations of rt-TDDFT simulations are used for the annealing simulations of picosecond atomistic dynamics.

Figure 3A shows the evolution of molecular production from annealed water plasma with an annealing rate of 1.0 K/fs (traj1 in Table S1). The particle number of each molecule exhibits an exponential evolution, demonstrating that the random recombination of radical particles accounts for the generation of stable gaseous molecules. When the system reaches the ultimate ambient conditions, the stable H_2, O_2, and H_2O_2 molecules are reserved in liquid water, consistent with experimental measurements.[14−16] In the system of 32 water molecules, the amount of H_2, O_2, and H_2O_2 molecules produced during the annealing process is 5, 2, and 1, respectively. According to the above results, the overall reaction of liquid water under the irradiation of the intense laser can be expressed as

$$H_2O \rightarrow H_2 + \frac{1}{2}O_2 \quad (3)$$

$$2H_2O \rightarrow H_2 + H_2O_2 \quad (4)$$

Among them, reaction (3) is dominant.

Figure 3B shows the hydrogen yields from water plasma as a function of annealing rates with the same initial configuration (traj8 for each annealing rate in Table S1). It is obvious that the hydrogen production rate is proportional to the annealing rate. The time constant of free H^+ depletion is about 390 fs for the annealing rate of 2.0 K/fs (Figure S5), which is comparable to that of 198 fs in rt-TDDFT simulations. The annealing rate of 2.0 K/fs gives the fastest hydrogen production rate of ∼2 molecules/ps, which reflects the faster evolution along the free energy profiles. Interestingly, the highest hydrogen yield of 4 hydrogen molecules during the annealing processes occurred at an annealing rate of 2.0 K/fs, which is 4-fold higher than that at 0.2 K/fs. The yields increase with cooling rates confirms the gas formation mechanisms of random combinations of adjacent free radicals. We note that the slow cooling rate leaves the system in its high-energy state at the initial stage of annealing processes, and transient H_2 molecules may exist (Figure 3B).

To directly illustrate the recombination processes, the temporal evolution of distances between two adjacent hydrogen ions is tracked during ultrafast annealing in Figure 3C, and the H1 and H2 ions have an initial distance of 1.24 Å. With v_a = 0.2 K/fs, the high ionic temperatures lead to the fast movement of two hydrogen ions. The weak bonding does not constrain the two hydrogen ions, and they move apart despite the initial spatial neighboring. The two hydrogen ions are very likely to recombine with the O* or OH* to form more stable H_2O molecules. With a higher annealing rate of 0.5, 1.0, and 2.0 K/fs, the distance between two hydrogen ions gradually evolves to a constant value of ∼0.76 Å after initial bond length oscillations, which demonstrates the production of hydrogen molecules.[26] In addition, the H_2 formation process is much faster with a higher annealing rate, which is consistent with Figure 3B. For two hydrogen atoms (H3 and H4) with a large initial distance of 3.65 Å, the hydrogen molecule can only form with the fastest annealing rate of 2.0 K/fs as shown in Figure S6.

Figure 3D summarizes the average yields of various molecules under different annealing rates, which are obtained from eight annealing trajectories (Table S1). One can see that the production yields increase with annealing rate, and the average production of H_2, O_2, and H_2O_2 molecules at v_a = 1.0 K/fs are 3.25, 1.25, and 0.75, which are 4-fold, 5-fold, and twice as much as at v_a = 0.2 K/fs, respectively. The production yields of H_2 and O_2 are almost saturated at v_a = 2.0 K/fs. It is noteworthy that the production of H_2O_2 at 2.0 K/fs is twice as much as that at 1.0 K/fs, which is attributed to the faster cooling processes. Therefore, the adjustment of annealing rate can be employed to modulate the product selectivity and reaction pathways.

The ultrafast annealing processes drive the system to cool rapidly and constrain the systems at local energy minima with various active molecules. According to the product yields and the enthalpy changes of respective reactions, the absorbed photon-to-chemical (APTC) conversion efficiency can be estimated with the following formula

$$\eta_{\mathrm{APTC}}(\%) = \frac{\Delta E_{\mathrm{mol}}}{E_{\mathrm{absorb}}} \times 100\%$$

where ΔE_{mol} is the chemical energy change at 300 K and E_{absorb} ≈ 106.5 eV is the total energy absorbed by the system with the electric field strength E_0 = 2.4 V/Å and wavelength λ = 800 nm. The η_{APTC} increases almost linearly with the annealing rate from 2.9% at 0.2 K/fs to 9.2% at 1.0 K/fs and reaches 12.1% at v_a = 2.0 K/fs (Figure S7 and Table S2). Experimentally, an efficiency of 2.1% is obtained at a slower annealing rate of 1×10^{-5} K/fs.[25] It is noted that the intense expansion and carrier diffusion are highly efficient for active species to survive, and they enhance the secondary reactions of gas formation,[12,27,28] which are hard to include in present quantum mechanics simulations with a finite supercell size. The fast annealing rate in simulations compensates for these effects and gives rise to reasonable efficiency.

https://doi.org/10.1021/acs.nanolett.4c02996
Nano Lett. 2024, 24, 12799−12805

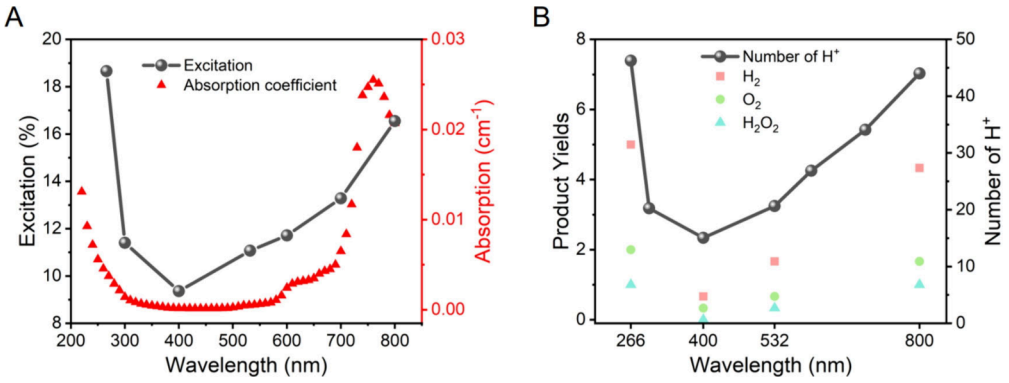

Figure 4. Effect of the wavelength on water plasma generation and molecular production efficiencies. (A) The excited valence electrons (black dot) at t = 50 fs in nonadiabatic simulations are a function of wavelength. The electronic excitations match well with the absorption coefficients of liquid water (red triangle). Experimental data are taken from ref 30. (B) The final product yields and number of H^+ are at 50 fs under the laser irradiations of different wavelengths.

As hydrogen production is attributed to photoinduced water plasma and subsequent annealing processes, the modulation of plasma generation is supposed to affect the hydrogen production efficiency. There are many factors that can affect the efficiencies of water plasma generations, such as laser wavelength, pulse duration, repetition rate, spot size, state of the sample (gas, cluster or liquid), surrounding environments, and external conditions.[23] The optical absorption efficiency is dependent on the wavelength of laser pulses, thus determining the thermodynamic properties of the generated water plasma. The impact ionization can take place during the irradiation of long laser pulses, leading to the strong absorption of the later part of laser pulses, and the high repetition rate may lead to the heat accumulations between consecutive pulses. The small spot size corresponds to the large specific surface area of generated water plasma, which accelerates the diffusion processes and enhances the heat dissipation and annealing rate. The initial state (gas, cluster, or liquid) and possible solutes can also affect the thermodynamic evolution of systems. The surrounding environments, e.g., heterogeneous interfaces, modulate the generations and states of water plasma by field enhancement effects, photocarrier transfer, and heat dissipation.[26,29] Other external conditions, e.g., electric and magnetic fields, directly affect the diffusions of photocarriers and transient species, affecting the thermodynamic properties of highly ionized water plasma.

Here, we consider the influence of laser wavelength on the generation of nonequilibrium water plasma, and the wavelength from 266 to 800 nm is chosen. Figure 4A shows the effective proportion of excited electrons in liquid water as a function of the laser wavelength. The tunneling ionization is demonstrated to account for the electronic excitation of ∼16% valence electrons with the wavelength of 800 nm,[13] and the 266 nm laser pulses can lead to the strong single-photon excitation of ∼19% valence electrons due to above-gap photoabsorption. Therefore, both laser pulses lead to intense electronic excitations and water plasma generation (Figure S8A and Figure 2B). On the other hand, an excitation minimum of ∼9% is obtained at the wavelength of 400 nm, and the bandgap is closed owing to structural distortions (Figure S8B). We note that the electronic excitations are well consistent with the experimental absorption spectrum of liquid water,[30] though the small redshift is observed due to a smaller theoretical bandgap of ∼4 eV. The strong electronic excitation leads to the breakdown of water molecules, and the fraction of free protons exhibits a similar profile with electronic excitation (Figure 4B).

Following the above annealing procedures, we annealed the water plasma induced by different laser wavelengths (800, 532, 400, and 266 nm) with an annealing rate of 1.0 K/fs. Figure 4B shows the yields of H_2, O_2, and H_2O_2 molecules under different laser-excited liquid water. One can see that the production yields of H_2, O_2, and H_2O_2 molecules exhibit nearly similar proportions of 5:2:1 regardless of the laser wavelength. Besides, the production yields exhibit a similar trend with electronic excitation and proton fraction. This indicates that the random states of photoinduced water plasma are strongly related to subsequent molecule production processes, demonstrating the random scattering and recombination mechanisms of molecular production. In the system of 32 water molecules, the hydrogen yield is 5 molecules for a 266 nm laser and 4.3 molecules for 800 nm, and even the minimum yield can reach 0.7 molecules for a 400 nm laser. Therefore, it has a great potential to utilize sunlight to generate hydrogen molecules via focusing sunlight in liquid water or driving water photosplitting with solar based lasers.

In conclusion, we reveal the microscopic mechanisms of direct hydrogen production in laser-induced water plasma with the combined nonadiabatic rt-TDDFT and T_i-based AIMD annealing simulations. The intense irradiation of laser pulses leads to water molecule dissociation into various active ions and radicals, resulting in the generation of nonequilibrium water plasma. The subsequent random scattering and recombination of active species during the annealing processes lead to the formation of various molecules, including H_2, O_2, and H_2O_2. The fast annealing rate ν_a significantly increases the hydrogen production yields and suppresses the active particles from recombining back into water molecules. Besides, the adjustment of annealing rates is shown to modulate the production ratios and reaction pathways. The calculated photo-to-chemical conversion efficiency is 9.2% at ν_a = 1.0 K/fs. In addition, the laser wavelength can affect the efficiency of water plasma generation and the subsequent molecule formation. This work not only demonstrates a novel and green method for efficient hydrogen production without catalyst but also offers new insights into the fundamental chemical processes during plasma generation and subsequent ionic dynamics.

https://doi.org/10.1021/acs.nanolett.4c02996
Nano Lett. 2024, 24, 12799−12805

■ ASSOCIATED CONTENT

Supporting Information

The Supporting Information is available free of charge at https://pubs.acs.org/doi/10.1021/acs.nanolett.4c02996.

Detailed calculation method, electron excitation and temperature information on the system, detailed charge evolution and other ionic and molecular components during photoexcitation, the Gibbs free energy of the reaction with temperature, additional ion evolution and energy conversion efficiency at different annealing rates, density of states at different wavelengths, and the bond length distribution of H_2 and O_2, the specific number of products per trajectory at different annealing rates and wavelengths, and the energy conversion efficiencies data at different annealing rates (PDF)

■ AUTHOR INFORMATION

Corresponding Authors

Jiyu Xu − *Beijing National Laboratory for Condensed Matter Physics and Institute of Physics, Chinese Academy of Sciences, Beijing 100190, China; Songshan Lake Materials Laboratory, Dongguan, Guangdong 523808, China;* orcid.org/0000-0002-2628-5492; Email: jiyuxu@iphy.ac.cn

Cui Zhang − *Beijing National Laboratory for Condensed Matter Physics and Institute of Physics, Chinese Academy of Sciences, Beijing 100190, China; Songshan Lake Materials Laboratory, Dongguan, Guangdong 523808, China;* orcid.org/0000-0002-2154-5187; Email: cuizhang@iphy.ac.cn

Sheng Meng − *Beijing National Laboratory for Condensed Matter Physics and Institute of Physics, Chinese Academy of Sciences, Beijing 100190, China; School of Physical Sciences, University of Chinese Academy of Sciences, Beijing 100049, China; Songshan Lake Materials Laboratory, Dongguan, Guangdong 523808, China;* orcid.org/0000-0002-1553-1432; Email: smeng@iphy.ac.cn

Enge Wang − *Beijing National Laboratory for Condensed Matter Physics and Institute of Physics, Chinese Academy of Sciences, Beijing 100190, China; Songshan Lake Materials Laboratory, Dongguan, Guangdong 523808, China; International Center for Quantum Materials School of Physics, Peking University, Beijing 100871, China;* Email: egwang@pku.edu.cn

Authors

Qunfang Gu − *Beijing National Laboratory for Condensed Matter Physics and Institute of Physics, Chinese Academy of Sciences, Beijing 100190, China; School of Physical Sciences, University of Chinese Academy of Sciences, Beijing 100049, China*

Yimin Zhang − *Key Laboratory of Material Physics, Ministry of Education, School of Physics and Microelectronics, Zhengzhou University, Zhengzhou 450001, China*

Daqiang Chen − *Beijing National Laboratory for Condensed Matter Physics and Institute of Physics, Chinese Academy of Sciences, Beijing 100190, China; School of Physical Sciences, University of Chinese Academy of Sciences, Beijing 100049, China;* orcid.org/0000-0003-1461-7135

Luhao Zhang − *International Center for Quantum Materials School of Physics, Peking University, Beijing 100871, China; Beijing National Laboratory for Condensed Matter Physics and Institute of Physics, Chinese Academy of Sciences, Beijing 100190, China*

Complete contact information is available at: https://pubs.acs.org/10.1021/acs.nanolett.4c02996

Author Contributions

#Q.G. and Y.Z. contributed equally to this work. S.M. and J.X. conceived the project. S.M., J.X., E.W., and C.Z. supervised the project. Q.G. carried out the rt-TDDFT and *ab initio* molecular dynamics simulations. Q.G., D.C., Y.Z., and J.X. analyzed the data. L.Z. participated in discussions. Q.G., J.X., Y.Z., and S.M. wrote the manuscript, and all authors approved the final version.

Notes

The authors declare no competing financial interest.

■ ACKNOWLEDGMENTS

We acknowledge financial support from the National Natural Science Foundation of China (No. 12025407, No. 12304351, No. 11934003, and No. 12204513), Ministry of Science and Technology (No. 2021YFA1400201), Chinese Academy of Sciences (No. YSBR047 and No. XDB330301), and Postdoctoral foundation of Henan Province (HN2024068).

■ REFERENCES

(1) Dawood, F.; Anda, M.; Shafiullah, G. M. Hydrogen production for energy: An overview. *Int. J. Hydrog. Energy* **2020**, *45*, 3847−3869.

(2) Nishiyama, H.; et al. Photocatalytic solar hydrogen production from water on a 100-m^2 scale. *Nature* **2021**, *598*, 304−307.

(3) Abdin, Z.; et al. Hydrogen as an energy vector. *Renew. Sust. Energy Rev.* **2020**, *120*, 109620−109652.

(4) Schmidt, O.; et al. Future cost and performance of water electrolysis: An expert elicitation study. *Int. J. Hydrog. Energy* **2017**, *42*, 30470−30492.

(5) Bicer, Y.; Sprotte, A. F. V.; Dincer, I. Concentrated solar light splitting using cold mirrors for photovoltaics and photonic hydrogen production applications. *Appl. Energy* **2017**, *197*, 169−182.

(6) Safari, F.; Dincer, I. A review and comparative evaluation of thermochemical water splitting cycles for hydrogen production. *Energy Convers. Manage.* **2020**, *205*, 112182−112199.

(7) Wang, Q.; Domen, K. Particulate photocatalysts for light-driven water splitting: Mechanisms, challenges, and design strategies. *Chem. Rev.* **2020**, *120*, 919−985.

(8) Reilly, K.; Wilkinson, D. P.; Taghipour, F. Photocatalytic water splitting in a fluidized bed system: Computational modeling and experimental studies. *Appl. Energy* **2018**, *222*, 423−436.

(9) Nishioka, S.; Osterloh, F. E.; Wang, X.; Mallouk, T. E.; Maeda, K. Photocatalytic water splitting. *Nat. Rev. Methods Primers* **2023**, *3*, 42.

(10) Megía, P. J.; Vizcaíno, A. J.; Calles, J. A.; Carrero, A. Hydrogen production technologies: From fossil fuels toward renewable sources. A mini review. *Energy Fuels* **2021**, *35*, 16403−16415.

(11) Elkins, M. H.; Williams, H. L.; Shreve, A. T.; Neumark, D. M. Relaxation Mechanism of the Hydrated Electron. *Science* **2013**, *342*, 1496−1499.

(12) Loh, Z. H.; et al. Observation of the fastest chemical processes in the radiolysis of water. *Chem. Phys. Lett.* **2020**, *367*, 179−182.

(13) Xu, J.; Chen, D.; Meng, S. Probing laser-induced plasma generation in liquid water. *J. Am. Chem. Soc.* **2021**, *143*, 10382−10388.

(14) Chin, S. L.; Lagacé, S. Generation of H_2, O_2, and H_2O_2 from water by the use of intense femtosecond laser pulses and the possibility of laser sterilization. *Appl. Opt.* **1996**, *35*, 907−911.

(15) Maatz, G.; et al. Chemical and physical side effects at application of ultrashort laser pulses for intrastromal refractive surgery. *J. Opt. A: Pure Appl. Opt.* **2000**, *2*, 59−64.

(16) Kierzkowska-Pawlak, H.; Tyczkowski, J.; Jarota, A.; Abramczyk, H. Hydrogen production in liquid water by femtosecond laser-induced plasma. *Appl. Energy* **2019**, *247*, 24−31.
(17) Lian, C.; Zhang, S.-J.; Hu, S.-Q.; Guan, M.-X.; Meng, S. Ultrafast charge ordering by self-amplified exciton-phonon dynamics in TiSe2. *Nat. Commun.* **2020**, *11*, 43.
(18) Guan, M.; et al. Theoretical Insights into Ultrafast Dynamics in Quantum Materials. *Ultrafast Science* **2022**, *2022*, 9767251.
(19) Schaffer, C. B.; Nishimura, N.; Glezer, E. N.; Kim, A. M. T.; Mazur, E. Dynamics of femtosecond laser-induced breakdown in water from femtoseconds to microseconds. *Opt. Express* **2002**, *10*, 196−203.
(20) Basconi, J. E.; Shirts, M. R. Effects of Temperature Control Algorithms on Transport Properties and Kinetics in Molecular Dynamics Simulations. *J. Chem. Theory Comput.* **2013**, *9*, 2887−2899.
(21) Yan, B.; et al. Efficient and Rapid Hydrogen Extraction from Ammonia-Water via Laser Under Ambient Conditions without Catalyst. *J. Am. Chem. Soc.* **2024**, *146*, 4864−4871.
(22) Kao, P.-K.; VanSaders, B. J.; Glotzer, S. C.; Solomon, M. J. Accelerated annealing of colloidal crystal monolayers by means of cyclically applied electric fields. *Sci. Rep.* **2021**, *11*, 11042−11055.
(23) Vogel, A.; Noack, J.; Hüttman, G.; Paltauf, G. Mechanisms of femtosecond laser nanosurgery of cells and tissues. *Appl. Phys. B: Laser Opt.* **2005**, *81*, 1015−1047.
(24) Kaiser, A.; Rethfeld, B.; Vicanek, M.; Simon, G. Microscopic processes in dielectrics under irradiation by subpicosecond laser pulses. *Phys. Rev. B* **2000**, *61*, 11437−11450.
(25) Yan, B.; et al. Laser Direct Overall Water Splitting for H_2 and H_2O_2 Production. *Proc. Natl. Acad. Sci. U.S.A.* **2024**, *121*, No. e2319286121.
(26) Yan, L.; Xu, J.; Wang, F.; Meng, S. Plasmon-induced ultrafast hydrogen production in liquid water. *J. Phys. Chem. Lett.* **2018**, *9*, 63−69.
(27) Elles, C. G.; Jailaubekov, A. E.; Crowell, R. A.; Bradforth, S. E. Excitation-energy dependence of the mechanism for two-photon ionization of liquid H_2O and D_2O from 8.3 to 12.4 eV. *J. Chem. Phys.* **2006**, *125*, 044515−044527.
(28) Savolainen, J.; Uhlig, F.; Ahmed, S.; Hamm, P.; Jungwirth, P. Direct observation of the collapse of the delocalized excess electron in water. *Nat. Chem.* **2014**, *6*, 697−701.
(29) Li, Y.; et al. Pulsed laser induced plasma and thermal effects on molybdenum carbide for dry reforming of methane. *Nat. Commun.* **2024**, *15*, 5495.
(30) Smith, R. C.; Baker, K. S. Optical properties of the clearest natural waters (200−800 nm). *Appl. Opt.* **1981**, *20*, 177−184.

https://doi.org/10.1021/acs.nanolett.4c02996
Nano Lett. 2024, 24, 12799−12805